Simulation-Based Assessment of a Full-Scale Installed Quiet Landing Gear

Benjamin Duda[1]
Dassault Systèmes, D-80637 Munich, Germany

Ryan J. Ferris[2]
Dassault Systèmes, Long Beach, California, 90802, USA

Mehdi R. Khorrami[3]
NASA Langley Research Center, Hampton, Virginia, 23681, USA

   Full-scale simulations of a Gulfstream G-III aircraft, performed in support of the NASA Acoustic Research Measurements flights, are presented to complement results discussed in earlier studies. The flow solver employed in those studies, Dassault Systèmes' lattice Boltzmann PowerFLOW®, was also used during this investigation to conduct time-dependent simulations of the entire aircraft in landing configuration with a fully dressed landing gear. The high-fidelity simulations, performed at a Mach number of 0.23 and a Reynolds number of 10.5×10^6 based on mean aerodynamic chord, captured all relevant airframe noise sources. The computations were used to assess the aeroacoustic performance of the main landing gear, with and without noise reduction fairings installed, of a G-III aircraft equipped with Adaptive Compliant Trailing Edge technology and conventional Fowler flaps. To facilitate comparison of predicted noise signatures with effective perceived noise levels obtained from flight test measurements, the "as-flown" nose landing gear geometry, missing in our earlier studies, was added to the simulated G-III aircraft configurations. The high fidelity, synthetic data were post-processed using a Ffowcs-Williams and Hawkings integral approach to estimate farfield acoustic behavior, with pressures on the model solid surface or pressure and velocity components on a permeable surface enveloping the acoustic near field used as input.

I. Nomenclature

C_p	=	Pressure coefficient
D	=	Main landing gear wheel diameter
Re	=	Reynolds number based on mean aerodynamic chord
δ_f	=	Flap deflection angle

Acronyms

DNS	=	Direct Numerical Simulation
EPNL	=	Effective Perceived Noise Level
ERA	=	Environmentally Responsible Aviation
FDC	=	Flight Demonstrations and Capabilities
FWH	=	Ffowcs-Williams and Hawkings
LBM	=	Lattice Boltzmann Method
MLG	=	Main landing gear

[1] Senior Technical Specialist, Simulia A&D.
[2] Solution Consultant Specialist, Simulia A&D, Member AIAA.
[3] Aerospace Engineer, Computational AeroSciences Branch, Associate Fellow AIAA.

NLG = Nose landing gear
PNL = Perceived Noise Level
PNLT = Tone-corrected PNL
PSD = Power Spectral Density
VLES = Very Large Eddy Simulation

II. Introduction

Excessive exposure to aircraft noise can adversely affect the quality of life of communities living near major airports [1]. The introduction of commercial fleets with substantially quieter and more fuel-efficient aircraft is essential if civil aviation is to expand at the rate necessary to meet the anticipated growth in global air traffic [2]. Mitigation of aircraft noise remains a critical goal of the NASA Aeronautics Research Mission Directorate (ARMD). Although most efforts initially focused on reduction of propulsion noise, the airframe component of the generated sound has received much attention in recent years due to its prominence during aircraft approach and landing.

Development and maturation of viable airframe noise reduction (NR) technologies was vigorously pursued under the Environmentally Responsible Aviation (ERA) project [3]. This effort culminated with the evaluation of flap and landing gear NR technologies via flight testing under the Flight Demonstrations and Capabilities (FDC) project of ARMD [4] [5]. Equally important, advancement and validation of system-level, simulation-based airframe noise prediction methodologies that could handle the extreme geometrical complexities and their intricate, time-dependent flow fields – responsible for sound generation – was initiated under ERA [6], [7], [8] and is being continued as a critical element of the FDC project [9], [10].

NASA evaluated the aeroacoustic performance of several airframe NR technologies installed on a Gulfstream-III (G-III) aircraft during the Acoustic Research Measurements (ARM) flight test campaign. The first test (ARM-I, 2016) evaluated the Adaptive Compliant Trailing Edge (ACTE) concept as a means to alleviate the noise produced by the wing flaps [4], [5]. The second test (ARM-II, 2017) targeted main landing gear (MLG) and gear cavity NR treatments in combination with the ACTE technology [4], [5]. For the third flight test (ARM-III, 2018), the ACTE flaps were removed and the original Fowler flaps were reinstalled on the G-III aircraft to obtain baseline flap and landing gear data, and to assess the noise reduction capability of the landing gear technologies for conventional flaps [4]. In support of the ARM-I and ARM-II tests, our previous computational studies targeted the configurations that were being tested, namely, the ACTE-equipped G-III with and without the NR fairings installed on the main landing gear [10], and the G-III aircraft with its Fowler flaps deflected at 20° and MLG deployed. This latter configuration served as a baseline to gauge the aeroacoustic performance of the ACTE technology and landing gear fairings [9]. A thorough comparison between predicted (synthetic) and measured phased microphone array data yielded very good agreement for their respective integrated farfield noise spectra [11]. To reduce computational resources and expedite time-to-solution, the nose landing gear (NLG) was omitted in our previous simulations. As a result, direct comparisons between predicted and measured Effective Perceived Noise Levels (EPNL), an important noise metric used by industry to determine the effectiveness of a given NR technology, would have been questionable at best.

The present computational study is a continuation of our previous efforts. To facilitate validation of predicted farfield noise spectra and EPNL values, a high-fidelity replica of the "as flown" nose landing gear was developed and integrated into the simulated G-III geometry. With the addition of the nose gear, the focus of the present study are those G-III configurations that were flight-tested during the ARM-III campaign: Fowler flaps deflected at 20° and 39° with and without MLG fairings installed.
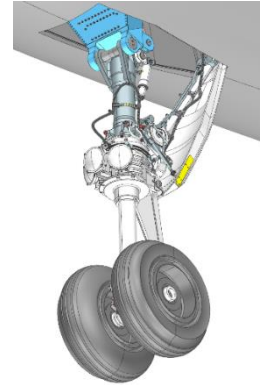
III. Aircraft Model

The processes used to develop the high-fidelity digital models that replicate most of the geometric detail of the "as flown" G-III testbed, including flaps (Fowler and ACTE) and MLG with and without fairings, are presented in Refs. [9], [10]. Except for the nose landing gear, the CAD model of the full-scale, full-span aircraft contained all the major components – fuselage, wing with deflected flaps including brackets, tail, flow-through nacelle with hush-kit, and main landing gear – of the actual testbed.

For the present computational study, a highly defined CAD model of the nose landing gear, including its cavity, was developed from carefully conducted laser scans of the component while the aircraft was placed on jacks to have the gear in the fully extended landing configuration. Significant effort was spent ensuring that the finest details of the nose gear exterior surfaces (i.e., outer mold lines) were captured accurately. The complete aircraft model, with nose landing gear integrated, is shown in Fig. 1. For an accurate representation of the aircraft in the simulation, a triangular surface mesh is created by tessallating the elements of the CAD model using PowerDELTA®.
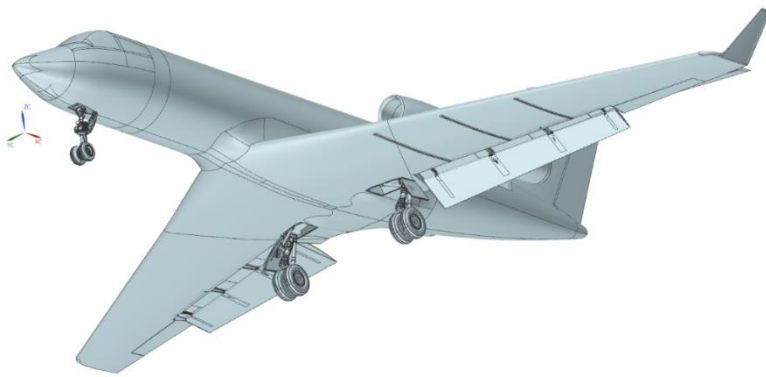
a) Aircraft with nose landing gear integrated   **b) Close-up view of nose gear**

Fig. 1 Gulfstream G-III aircraft CAD model.

IV. Computational Approach

The numerical simulations were performed using Dassault Systèmes' PowerFLOW® solver, which is based on the three-dimensional, 19-state (D3Q19) lattice Boltzmann method (LBM) [12], [13], [14], [15]. LBM has been extensively validated for a wide variety of applications ranging from academic direct numerical simulation (DNS) cases to industrial flow problems in the fields of aerodynamics [16] and aeroacoustics [6], [17], [18]. At a macroscopic level, LBM uses a simpler and more general physics formulation than methods based on the Navier-Stokes equations [12]. The LBM equations recover the macroscopic hydrodynamics of the Navier-Stokes equations through the Chapman-Enskog expansion [19], [20].

The local formulation of the LBM equations allows a highly efficient implementation for distributed computations on thousands of processors. The low dissipation and dispersion properties of the numerical scheme typically produce aerodynamic and aeroacoustic results that are comparable to those obtained with classical CFD solvers that use higher-order large eddy simulation (LES).

A. Turbulence Modeling

The lattice Boltzmann flow simulation is equivalent to a DNS of the flow. For high Reynolds number (Re) flows, such as those addressed in this work, the lattice Boltzmann Very Large Eddy Simulation (LB-VLES) approach is used to reduce computational resource requirements [14], [21]. This means that turbulence is modeled in areas of attached flow such as boundary layers, but resolved in wakes or regions of detached flows.

B. Wall Treatment

The standard lattice Boltzmann bounce-back boundary condition for the no-slip condition or the specular reflection for the free-slip condition are generalized through a volumetric formulation [12], [13] near the wall for arbitrarily oriented surface elements (surfels) within the Cartesian volume elements (voxels). This formulation of the boundary condition on a curved surface cutting the Cartesian grid is automatically mass, momentum, and energy conservative while maintaining the general spatial second-order accuracy of the underlying LBM numerical scheme. To reduce the resolution requirements near the wall for high Re flows, a hybrid wall function is used to model the region of the boundary layer closest to the solid surfaces [16], [22].

C. Volume Meshing

The lattice Boltzmann approach is solved on voxels where variable resolution (VR) regions can be defined to allow for local mesh refinement by successive factors of two. Based on the facetized geometry and the local volume resolution, the model surface is discretized by planar surfels. This process allows the automatic generation of computational grids for any arbitrarily complex geometrical shapes. Except for the regions surrounding the nose landing gear and its wake, the meshes created in this study are identical to the ones used in the previous simulations for the Fowler and the ACTE flap configurations, cf. [8] and [9]. Fig. 2 shows the volume mesh created in the vicinity of the nose landing gear. Care was taken to sufficiently resolve geometric and flow features.
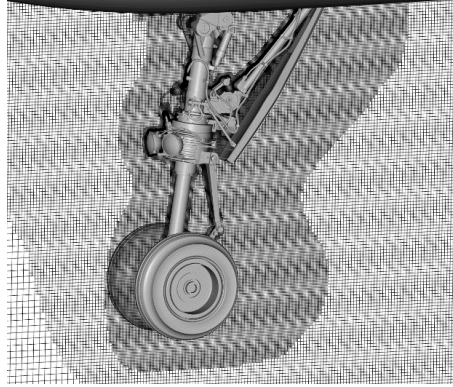
Fig. 2 Volume mesh in the vicinity of the nose landing gear, only every 2nd line shown.

D. Simulation Setup

Like the precursor study without the nose landing gear, simulations were performed at full scale with free-air boundary conditions at a Mach number of 0.23 and a Reynolds number of 10.5×10^6 based on a mean aerodynamic chord of 13.78 ft (4.2 m) and an aircraft speed of 150 knots. This Re represents a value that is close to 60% of the flight Reynolds number; thus, it is sufficiently high to produce farfield noise levels that are nearly equivalent to those obtained at full flight but at a lower cost. The simulation domain was initialized with free flow conditions except in the immediate near field region around the aircraft, where zero flow velocity and free stream pressure were specified. The first ~0.60 s of the transient simulations were discarded to remove any artifacts from initialization. The simulations were then run for another ~1.55 s of physical time, during which various data were recorded for post-processing.

The simulation campaign replicated flight tests for the landing aircraft. For this reason, a different angle of attack was simulated depending on the flap settings: $\alpha = 5°$ for a Fowler flap deflection of 20°, $\alpha = 2.85°$ for a Fowler flap deflection of 39° and $\alpha = 4.65°$ for an ACTE flap deflection of 25°.

E. Measurement Entities for Farfield Noise Propagation

Since the main goal of this study is to predict farfield noise levels, Dassault Systèmes' farfield noise solver PowerACOUSTICS® was used to obtain synthetic pressure signals at defined locations far away from the aircraft. An acoustic analogy approach based on the Ffowcs-Williams and Hawkings (FWH) formulation [23] was used here with the efficient and well-validated formulation developed by Farassat [24], also known as formulation 1A. The formulation is extended to account for uniform mean flow convection effects to simulate the noise generated and measured in an ideal infinite wind tunnel [25].

The input for the FWH computations are either a pressure dataset obtained on the geometry or a pressure and velocity dataset obtained on a permeable surface around the geometry. Since the NLG is rather isolated from other noise producing components, two different sets of permeable surfaces were created. This allows the measurement of farfield characteristics for the nose landing gear only. The resulting surfaces are shown in Fig. 3, where multiple endcaps are included to filter out hydrodynamic pressure fluctuations created by the wakes.
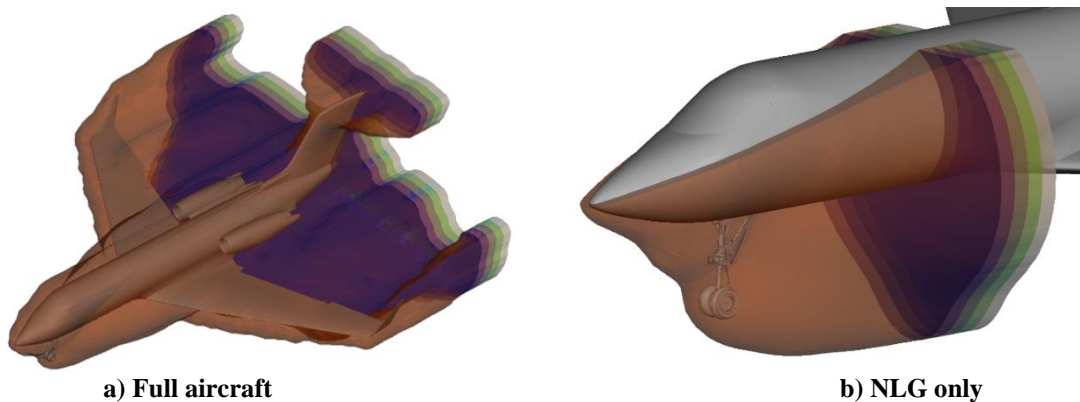

a) Full aircraft   **b) NLG only**

Fig. 3 Permeable measurement surfaces for FWH computation, shown with multiple end caps.

In order to replicate the isolated farfield noise contribution of the NLG for the solid FWH approach, the input surfaces can be split. This is shown in Fig. 4, where the blue-colored surfaces of the NLG and the forward segment of the aircraft fuselage can be used as separate input to the FWH computation.
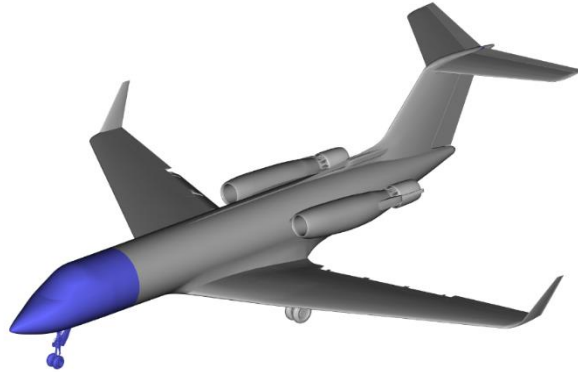

Fig. 4 Surfaces used for predicting isolated NLG contribution to farfield noise obtained with solid FWH formulation.

F. Effective Perceived Noise Level

The Effective Perceived Noise Level (EPNL) was calculated using a proprietary post-processing tool developed by Dassault Systèmes. The primary reference for the definition and calculation of EPNL is a publication of the ICAO [26]. The input to the tool is a semicircular arc of synthetic pressure signals obtained with FWH. Once a trajectory is determined, it is discretized into flight segments of a given duration, in this case 500 ms. For every flight segment, the emission time and position of the aircraft are determined, and a ray between the observer and aircraft is traced. The ray's intersection with the semicircular microphone array is found and a noise spectrum for the observer is formulated by interpolating the appropriate microphone's narrow-band spectra. For each flight segment, the spectrum at the observation point is corrected for distance, atmospheric absorption, Doppler shifting, and ground reflection. One-third octave sound pressure levels (SPL) are then computed and Perceived Noise Level (PNL) is calculated using the procedure described by the ICAO. Finally, tonal weighting and band sharing adjustments are made and EPNL is computed.

V. Numerical Results

A select number of configurations tested during the ARM-III campaign (Fowler flap-equipped G-III with/without MLG fairings) were simulated. Additionally, the NLG geometry was also added to the G-III aircraft with ACTE flaps.

A. Grid Resolution Study

In our previous study [9], the impact of grid resolution on the numerical solution was assessed for the Fowler flap configuration. This was done in a global manner, i.e., the edge length of each voxel was scaled consecutively by a factor of 1.5 to obtain three resolutions termed "coarse", "medium" and "fine". That study is replicated here and now includes the NLG. The resulting mesh sizes and required time steps are summarized in Table 1 for the Fowler Flap configuration. The ACTE configuration requires slightly less computational time due to the elimination of flap side edges and brackets, which typically require high resolution. At the submission deadline of this manuscript, the fine-resolution simulations were not yet completed. Only instantaneous aerodynamic and acoustic quantities are available for comparison because they require shorter physical simulation times for statistical convergence than the full record needed to reconstruct the farfield spectra in the desired frequency range.

Firstly, a comparison of pressure coefficients are presented in Fig. 5. Note from the figure that, as found in previous studies, surface pressures on the wing converge fast with increased spatial resolution and only small differences at the suction peaks are visible. Attention is now turned toward the NLG, where flow separations are highlighted by iso-surfaces of total pressure in Fig. 6. Here, small differences become visible depending on the resolution. This is expected because increased resolution will lead to the capture of smaller turbulent structures, which in turn can impact separation lines and mean flow.

Fig. 7 shows farfield spectra obtained with the solid and the permeable FWH computation for a flyover microphone located 120m below the aircraft. Due to insufficient time-dependent records from the ongoing fine-resolution simulation, only coarse and medium resolution results could be included here. Observe from the figure that increased

spatial resolution leads to additional content in the higher frequency range. Consistent with the findings in Ref. [10], this trend is expected to remain true for the fine simulation, as is the assumption that overall acoustic behavior was properly captured, up to 3 kHz, with the medium resolution results to be discussed in subsequent sections. Also note from Fig. 7 that the noise levels for the two FWH surfaces are similar in the mid-frequency range, but results obtained with the permeable FWH formulation show an earlier cut-off. This is a consequence of the lower spatial resolution of the flow field out to the permeable surface compared to the solid surface. The presence of tones can be observed, whose characteristics are dependent on the FWH formulation and the resolution. The lower frequency tone is due to a cavity mode that will be discussed in detail in section IV.B. The higher frequency tone stems from a hollow MLG post, which was described in Ref. [9] and identified to be sensitive to local flow and spatial resolution.

Table 1 Simulation metrics used to study spatial resolution effects on Fowler flap configuration with flap deflection angle $\delta_f = 39°$.

Resolution	Voxels [10^6]	Surfels [10^6]	Min Edge [10^{-4}m]	Timesteps	CPUh [10^6]
Coarse	1 711	41	7.2	2 293 760	0.2
Medium	5 436	72	4.8	3 440 640	1.2
Fine (not finished)	17 436	126	3.2	5 177 344	≈ 8.5

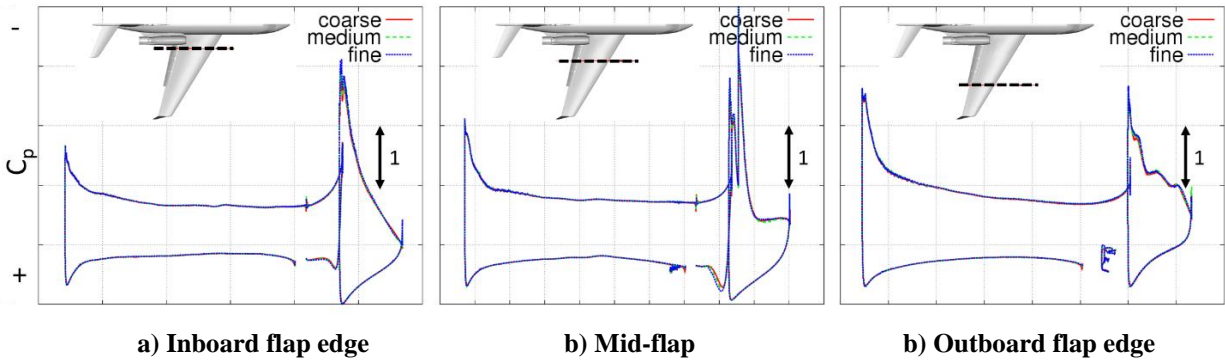a) Inboard flap edge   b) Mid-flap   b) Outboard flap edge

Fig. 5 Pressure distribution at three different spanwise locations for coarse, medium and fine simulation for Fowler flap deflection angle $\delta_f = 39°$.

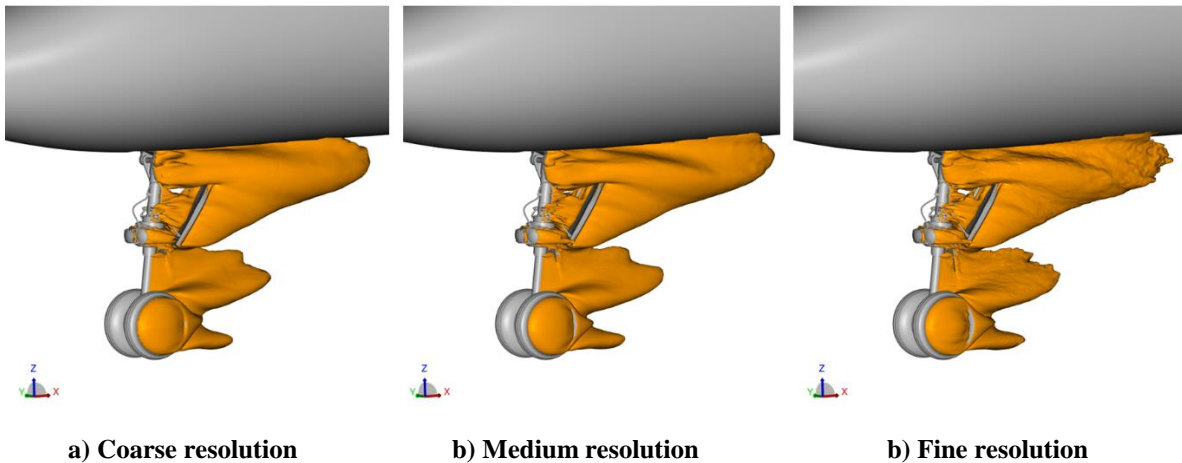a) Coarse resolution   b) Medium resolution   b) Fine resolution

Fig. 6 NLG wake comparing resolution levels

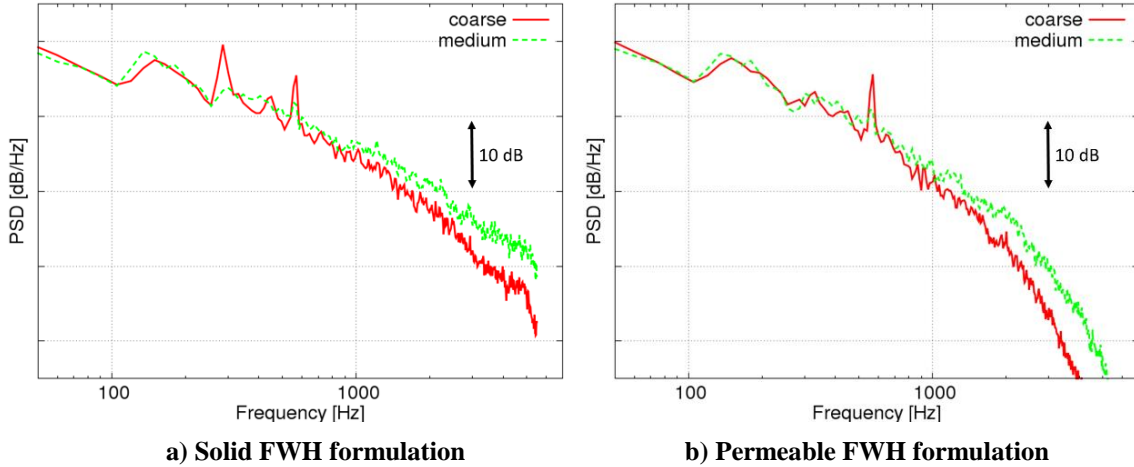**a) Solid FWH formulation** **b) Permeable FWH formulation**

Fig. 7 Power spectral density obtained with FWH formulation for coarse and medium simulations for flap deflection angle $\delta_f = 39°$.

B. Impact of NLG on Aerodynamics

The aerodynamic impact of the NLG on the downstream components of the aircraft is assessed in this section. A snapshot of the flow is given in Fig. 8, where resolved vortical structures are shown as isosurfaces of vorticity based on λ_2 criterion. As expected, the unsteady simulation resolves a large spectrum of turbulent structures as the flow passes over the nose landing gear. Since the mesh resolution is maintained downstream of the gear, turbulent wake structures are convected with the local flow and sustained over long distances. Observe from the figure that these structures impinge on the leading edge of the wing close to the fuselage junction and that the majority pass above the wing.

For a quantitative comparison of the flow field, two coarse simulations with a Fowler flap deflection of 20° were conducted at the same angle of attack; one without NLG and one with NLG. The additional computational cost for the latter is in the order of 10%. The resulting pressure distributions are shown in Fig. 9 for three different spanwise locations. The impact of the NLG is hardly discernable throughout the wing. To examine NLG effects on the flow field upstream of the MLG, contours of streamwise and spanwise velocity components on a spanwise plane 1.5 wheel diameters (D) upstream of the MLG are plotted in Fig. 10. The extracted velocity fields reveal that the portion of the NLG wake that does not pass over the wing occupies only a small region on the aircraft's underside. Due to the large distance between left and right MLGs, these components encounter a rather undisturbed flow. The same holds true for the inboard flap side edges, indicating that the impact of the NLG on the acoustics of the MLG and high lift system is minimal.
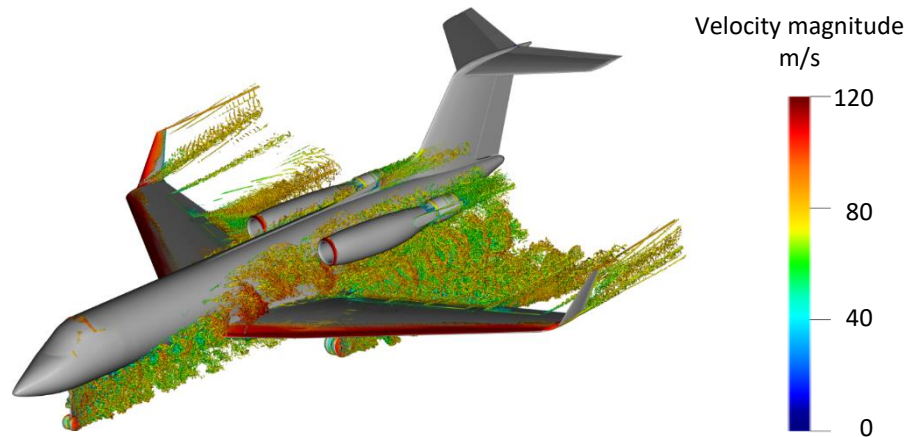

Fig. 8 Snapshot of resolved turbulent structure for Fowler flap deflection $\delta_f = 20°$ configuration with nose and main landing gear deployed, medium resolution.

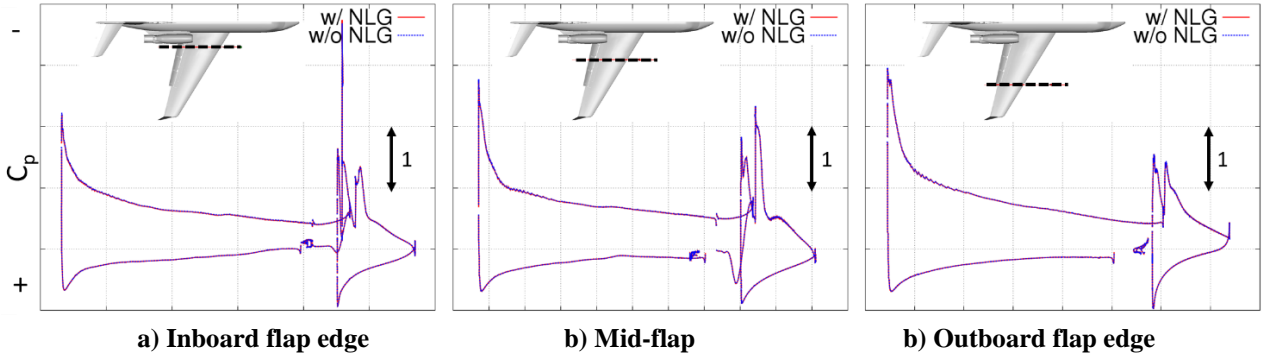a) Inboard flap edge   b) Mid-flap   b) Outboard flap edge

Fig. 9 Pressure distribution at three different spanwise locations for configuration with NLG and without NLG and Fowler flap deflection angle $\delta_f = 20°$.
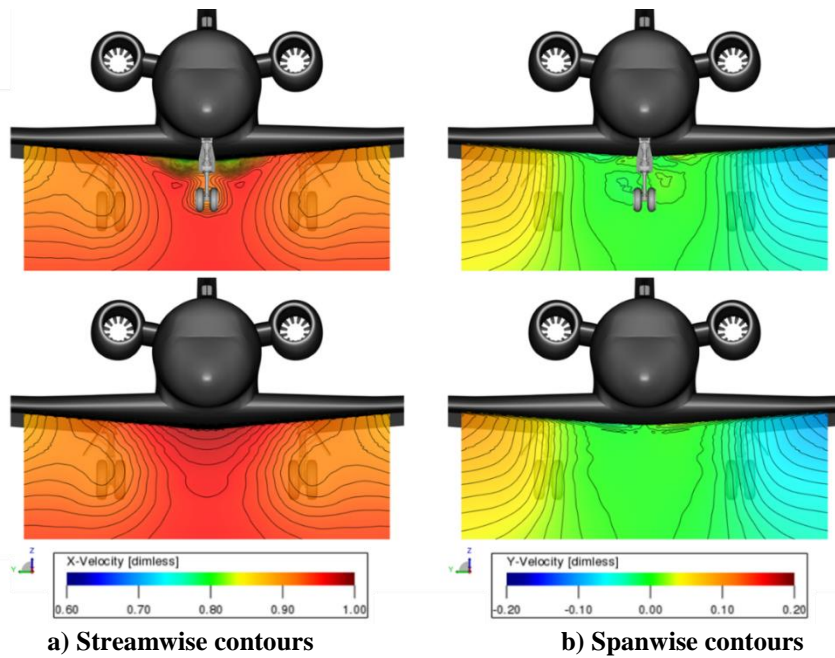

a) Streamwise contours   b) Spanwise contours

Fig. 10 Velocity contours for simulation with (top) and without (bottom) NLG on a plane 1.5 D upstream of MLG for a Fowler flap deflection $\delta_f = 20°$.

C. NLG Cavity Noise

Even though the NLG geometry was carefully scanned to reflect the flown geometry, the NLG cavity had to be geometrically approximated and subsystems inside the cavity (e.g., major linkages and hydraulic lines) have been omitted in this study. Similar to the MLG bay discussed in Ref. [8], an idealized (empty) cavity can lead to large resonances in a simulation. Certainly, this is a meaningful computational result for the modeled bay, but nonetheless undesirable since the real cavity either does not produce such tones or, if it does, they will be smeared and have low amplitudes due to the presence of the subsystems. For this reason, a sponge zone was applied to the ceiling of the cavity to dampen acoustics reflections for all configurations with landing gear deployed. The impact on farfield noise is shown in Fig. 11, which depicts coarse resolution results for a flyover microphone located 120m below the aircraft. The noise levels were computed with the solid FWH formulation and only the blue surfaces, cf. Fig. 4, were used as input to highlight the impact on NLG noise. A very strong cavity mode is seen with the first harmonic at about 270Hz. With inclusion of the sponge zone, the cavity mode is still present but pollution of the spectrum by higher harmonics in the mid-frequency range has been removed successfully.
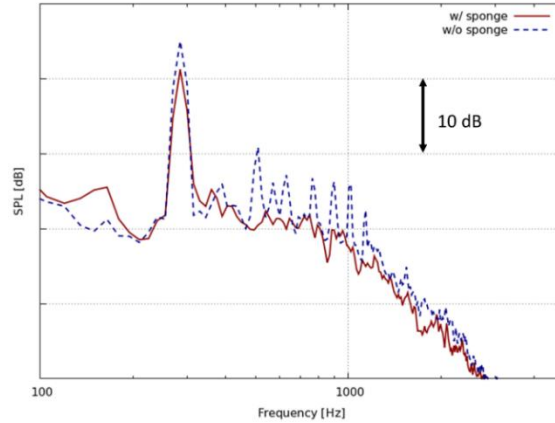
Fig. 11 NLG contribution to farfield noise levels at flyover microphone for coarse simulation with and without sponge zone in NLG cavity.

Since both solid and permeable FWH computations can be performed for the entire aircraft and the nose landing gear only, the corresponding spectra for the flyover microphone are shown in Fig. 12. Two prominent tones are visible, the lower one stemming from the above-mentioned cavity mode and the higher one from the hollow MLG front post. The striking difference between these two tones is that the former is visible only in the solid FWH formulation, while the latter is present independent of the FWH formulation.
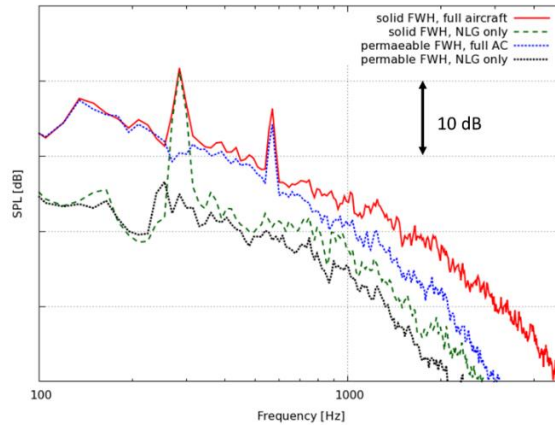
Fig. 12 Farfield noise levels at flyover microphone for full aircraft and isolated NLG obtained with solid and permeable FWH formulation.

The reason for this behavior has been investigated by creating the pressure dilatation field. Two snapshots with a time difference Δt equivalent to half the period of the cavity mode are presented in Fig. 13. Observe that strong and large pressure fluctuations are present inside the NLG cavity. Fig. 13b reveals, as expected, that the cavity mode has changed its phase by 180°. While this cavity mode leads to strong pressure fluctuations inside the cavity surface, the mode is trapped and hardly any fluctuations propagate outside. This means that the permeable surface, which is located away from the NLG, does not see these pressure fluctuations.

9
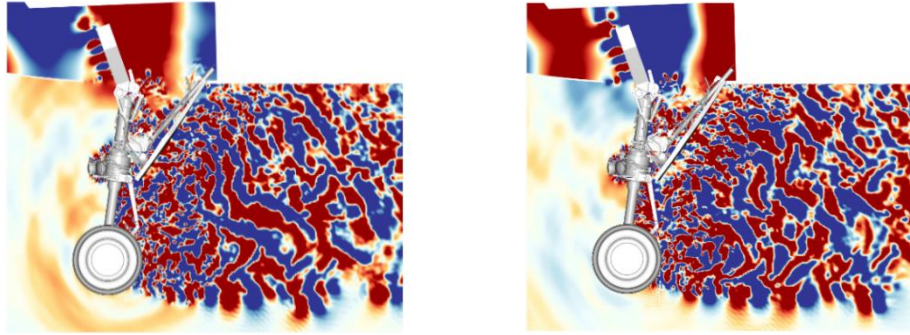
a) Streamwise contours at time t   **b) Streamwise contours at time t+Δt**

Fig. 13 Pressure dilatation field on aircraft symmetry plane at two different times showing a trapped NLG cavity mode.

D. Impact of NLG on Farfield Aeroacoustics

In order to assess the impact of the NLG on farfield acoustics, results from two medium resolution simulations are compared in this section. The first one is a Fowler flap configuration with a flap deflection $\delta_f = 20°$ with both MLG and NLG deployed. The second simulation, discussed in Ref. [8], is geometrically identical to the first one except for the NLG being retracted. A difference in angle of attack of $0.75°$ exists between the two simulated configurations, but it has been demonstrated that variations of a few degrees have little impact on farfield noise signatures [27].

Directivity contour maps are presented in Fig. 14. They have been computed from 360 microphones located on a semicircular arc with a radius of 120m centered on the aircraft in flyover direction. For consistency, only the solid FWH formulation has been used to compute the microphone signals. The left directivity map contains the results from the simulation with the NLG and the right directivity map contains the results from the simulation without the NLG. Note from Figs. 15a and 15b that adding the NLG to the configuration increases the SPL almost throughout the entire frequency and directivity ranges, as expected. The largest differences in SPL are seen in the low- to mid-frequency range at forward directivity angles. The global maximum around 300Hz between 0° and 40° for the simulation with NLG can be attributed to the NLG cavity tone, which is not present in the aft directivity angles. For a quantitative assessment, the differences in SPL between these simulations is plotted in Fig. 15. An increase of approximately 2 dB in the mid-frequency range is observed, which decreases for higher frequencies. Only for the low frequency region below 200Hz, a decrease caused by a small shift in cavity tones is visible.

Sample spectra are shown in Fig. 16 for the overhead position at 90°, highlighting that addition of the NLG increases SPL values in the mid frequency range by about 2 dB. Possible reasons for the reduced impact in the higher frequency range are insufficient spatial resolution in our simulations and/or the masking effect of MLG or flap side edge noise.
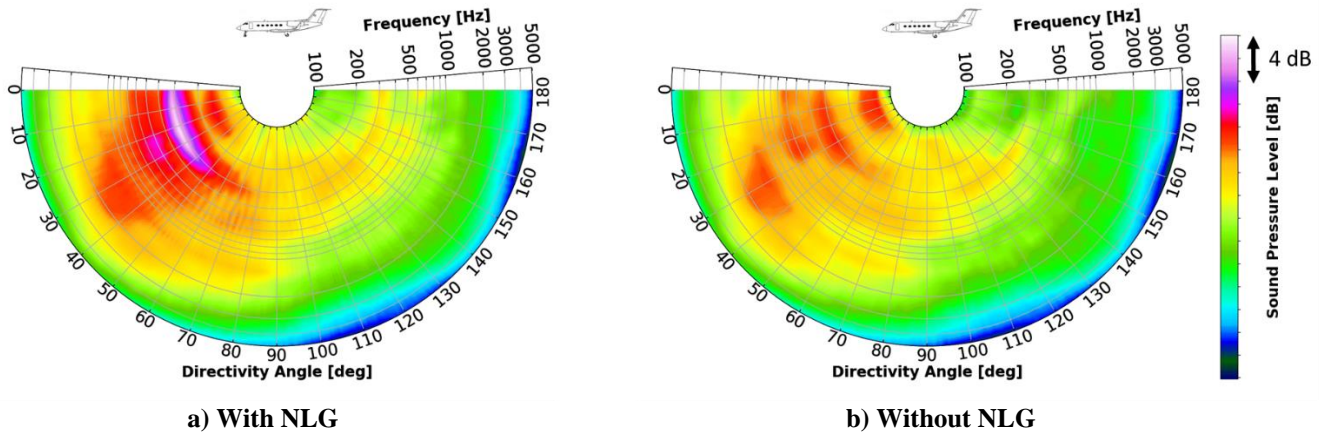

a) With NLG   **b) Without NLG**

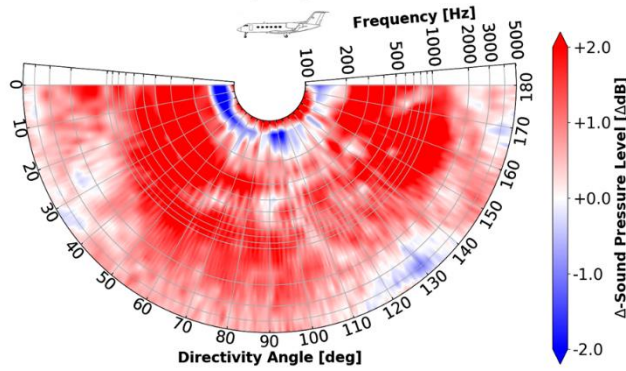**Fig. 14 Directivity contour maps in 1/3rd octave bands for Fowler flaps deflected 20°.**

Fig. 15 Differences in directivity contours for configuration with Fowler flaps deflected 20°, with and without NLG geometry.

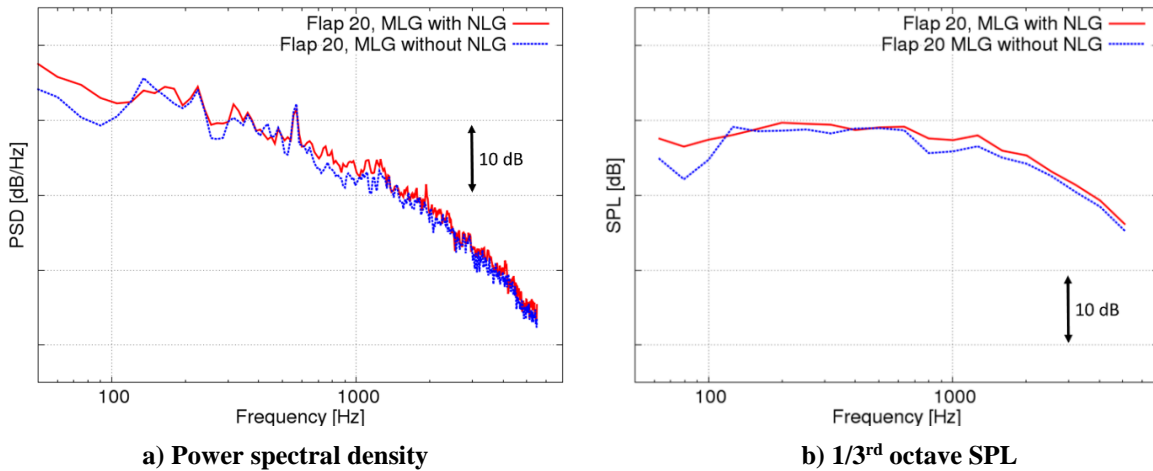| a) **Power spectral density** | b) **1/3rd octave SPL** |

Fig. 16 Spectral comparisons for Fowler flap configuration with and without NLG geometry.

As implied in section IV.E, in the FWH computation we can numerically remove the noise contribution of the NLG from a flow simulation where the NLG was geometrically present. The motivation is to compare the obtained noise levels (NLG1) with those of a flow simulation that did not contain the NLG geometry at all (NLG0). If these two results are quantitatively similar, then the NLG can be regarded as an isolated noise source with little interaction with MLG and flap side edge noise. The differences that resulted from subtracting NLG1 from NLG0, are shown in Fig. 17 for the configuration with Fowler flaps deflected 20°. The differences between these two results are within ±0.5 dB except for the low frequency range below 200 Hz. The larger differences could be caused by slight changes in the MLG cavity modes induced by the NLG wake. Overhead spectra are shown in Fig. 18, where the previous observation is confirmed: very small differences in the mid- to high-frequency range and larger differences in the very low-frequency range. Thus, the hypothesis that the NLG can be regarded as an isolated noise source for mid to high frequencies for this configuration and flow conditions is supported.
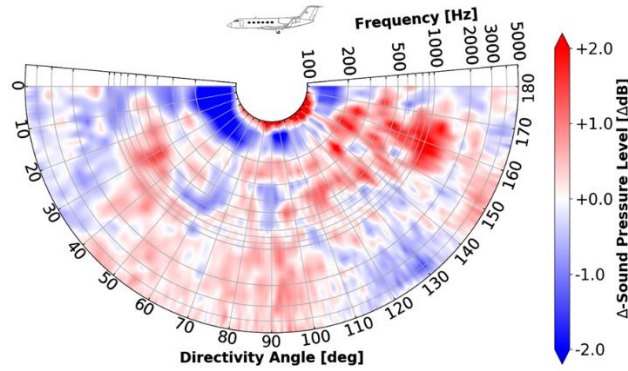
Fig. 17 Differences in directivity contours between a flow simulation where the NLG was present but its contribution removed in the FWH computation and a flow simulation where the NLG was not present.

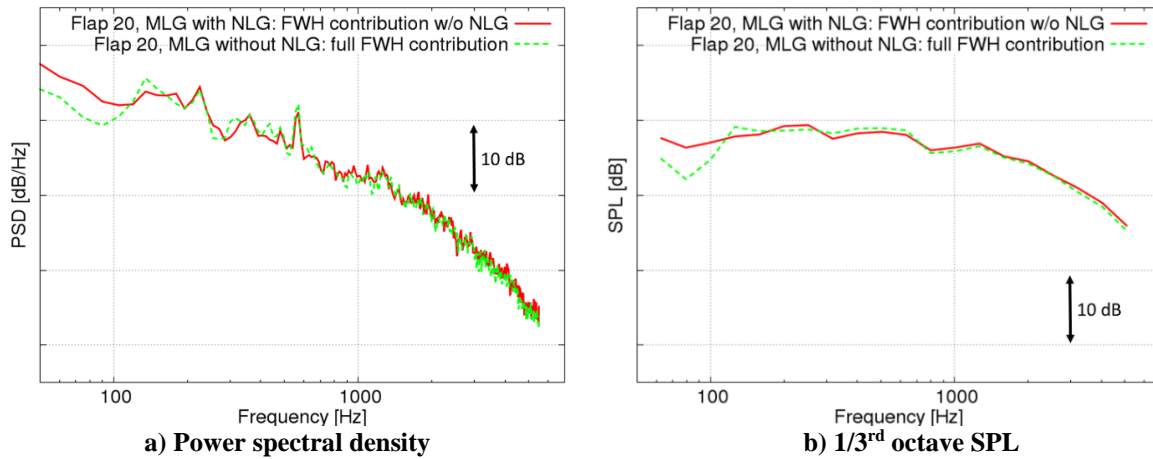a) **Power spectral density** b) **1/3rd octave SPL**

Fig. 18 Spectral comparisons of a flow simulation where the NLG contribution was removed in the FWH computation and a flow simulation where the NLG was not present.

F. Flyover Noise

The noise generated by the airframe was also analyzed from the standpoint of an observer on the ground as the aircraft passes overhead. We will discuss the tone-corrected Perceived Noise Level (PNLT) as a function of time as well as the overall Effective Perceived Noise Level (EPNL) in decibels (EPNdB). The calculation procedure for these two quantities can be found in Section IV.F. We will make determinations of differential PNLT and EPNL as a result of configuration changes in the following ways: 1) addition of the NLG, 2) use of both flap and landing gear noise reduction concepts in landing configuration, 3) aerodynamically equivalent configurations, and 4) use of MLG fairings for baseline flap configuration. The data presented here are based on the full aircraft solid measurement surface, as shown in Section IV.E, in medium resolution.

Simulations were also performed for the ACTE equipped G-III, $\delta_f = 25°$, with MLG deployed and porous MLG fairings installed, with and without NLG deployed. Fig. 19 shows the change in tone-corrected PNL (PNLT) values as the aircraft passes over the observer for these two configurations. The overall shape of the PNLT curve is similar, with an increase in noise levels throughout the aircraft's trajectory caused by the deployed NLG. This indicates that the additional noise content generated by the NLG is not necessarily dominant in a single directivity, as was also shown in the contour maps of Fig. 15. Looking at the change in PNLT$_{max}$ between the two configurations, an increase of approximately 3.7 dB is recognized with the addition of the NLG and its cavity to the aircraft geometry. EPNL also increased by 3.2 EPNdB. Although aircraft noise reduction is a system-level endeavor, the component-level results of the previous subsection showed that the overall noise contribution from the NLG is rather isolated. Thus, we may infer that the increase in EPNdB from NLG deployment can be offset by adding the porous MLG fairings: the decrease

in flyover noise associated with the fairings [10] is approximately equal to the increase from NLG deployment shown here.

Of interest to the present study was the determination of overall total noise reduction of the G-III in landing configuration as a result of the flap and MLG NR technologies. The Baseline G-III aircraft considered is that with the Fowler Flap δ_f = 39°, MLG/NLG deployed, and without porous MLG fairings installed. The G-III with NR concepts considered is that with the ACTE Flap δ_f = 25°, MLG/NLG deployed and with porous MLG fairings installed. From the PNLT curve in Fig. 20, we observe that most of the noise reduction occurs as the aircraft is approaching and is directly overhead, with PNLT$_{max}$ having been reduced by approximately 7.2 dB. A corresponding decrease in EPNL was also about 7.1 EPNdB. The largest change in PNLT is identifiable immediately before and after the baseline G-III aircraft travels overhead, indicating that the NR technologies not only affect the overall sound level but also alter the characteristic of the sound reaching the observer.
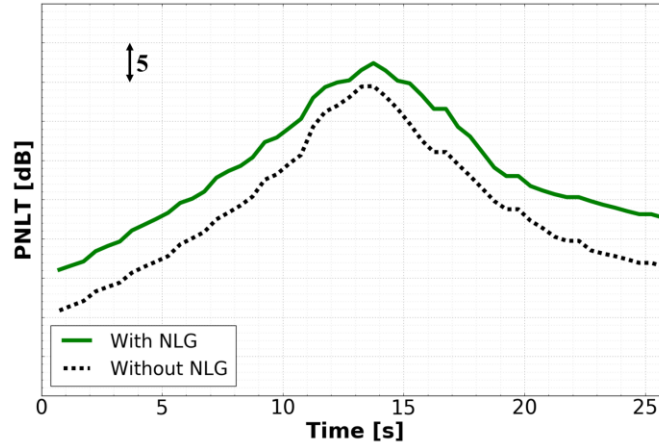

Fig. 19 Effect of NLG deployment on the PNLT time history of a G-III in landing with NR concepts installed (ACTE δ_f = 25° with MLG deployed and porous MLG fairings).
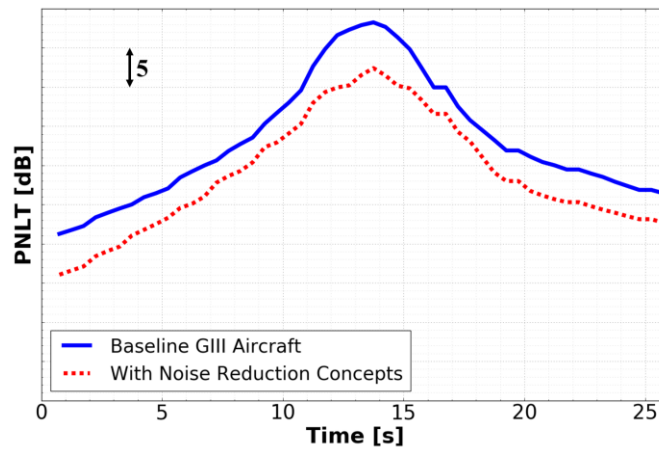

Fig. 20 Effect of NR technologies on the PNLT time history of a G-III in landing. Baseline: Fowler δ_f = 39°, MLG/NLG deployed, without porous MLG fairings; treated: ACTE δ_f = 25°, MLG/NLG deployed with porous MLG fairings.

The change in flap system from Fowler to ACTE led to a reduction in aerodynamic performance with flaps deployed, as established in [10]. Since airframe noise from lifting surfaces, such as flaps, is proportional to the magnitude of lift generated, a brief investigation was undertaken to quantify noise from aerodynamically equivalent configurations. To reduce the lift created by the Baseline G-III aircraft (Fowler δ_f = 39°, MLG/NLG deployed, and without porous MLG fairings installed), the Fowler flap deflection was decreased from 39° to 20° while leaving other settings the same (now labeled Baseline G-III Aircraft – Aero Equivalent). The PNLT time histories for this

configuration and the equivalent ACTE with flaps deflected 25° and porous MLG fairings installed are shown in Fig. 21. Observe that the flap and MLG NR concepts tested reduced $PNLT_{max}$ by 4.2 dB while reducing EPNL by 4.6 EPNdB.

The PNLT time histories for the two configurations of Fowler flaps deflected 20°, MLG/NLG gear deployed with and without porous MLG fairings are compared in Fig. 22. The plot demonstrates the acoustic performance of MLG fairings in conjunction with a conventional Fowler flap system. As shown in the figure, application of the MLG fairings decreased PNLT values between 1 and 2 dB over the entire period, resulting in an EPNL reduction of 1.2 EPNdB.
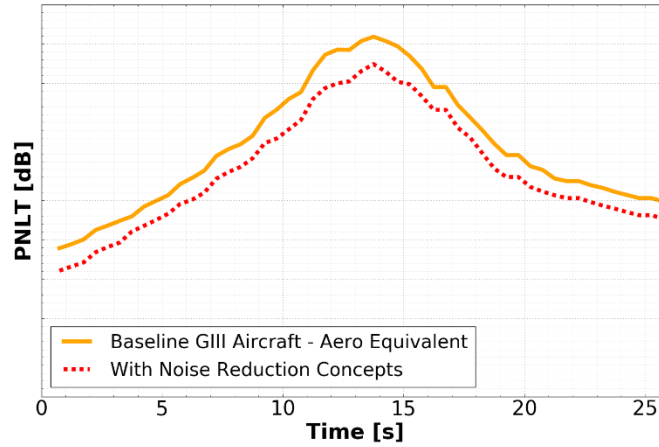

Fig. 21 PNLT time histories for the aerodynamically equivalent Baseline G-III (Fowler δ_f = 20°, MLG/NLG deployed, without porous MLG fairings) and the acoustically treated G-III (ACTE δ_f = 25°, MLG/NLG deployed with porous MLG fairings)
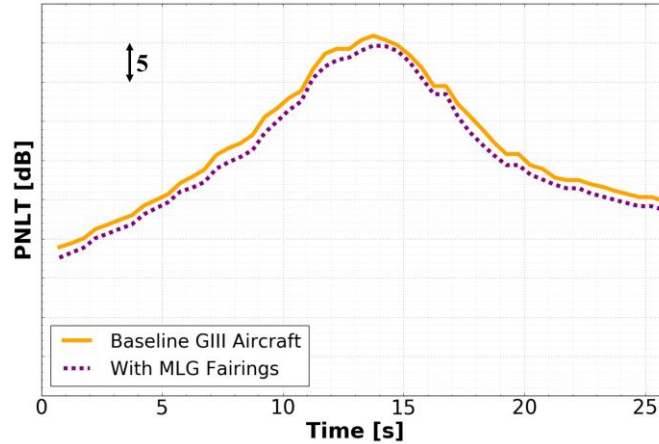

Fig. 22 PNLT time histories for Fowler flap 20°, MLG/NLG deployed with and without porous MLG fairings.

VI. Concluding Remarks and Outlook

A simulation campaign was conducted for a full G-III in landing configuration where, in contrast to previous simulations, a highly detailed NLG was included. The simulations were done for the aircraft equipped with conventional Fowler and ACTE flaps set at various deflection angles. Flight conditions were chosen to match flight tests. Although fine resolution simulations had not been completed by the time this report was submitted, a spatial resolution study indicated that aerodynamic quantities converged fairly quickly.

The impact of the NLG on both aerodynamics and acoustics was investigated. The aerodynamic effect was minor, since the wake from the NLG passed mostly over the wing without interacting with the MLG due to the relatively large distance between its port and starboard components. We showed that including an empty NLG cavity can lead to high-amplitude tones and that those can be alleviated with numerical damping inside the cavity without impacting

the noise characteristics of the NLG itself. Different strategies for obtaining farfield noise were investigated, with the outcome that the noise contribution of the NLG can be isolated from other prominent airframe sources. This is due to the large distance that exists between the NLG and the MLG and flap side edges. By adding the NLG, an increase of about 2 dB is observed for all directivity angles in the mid-frequency range. The impact decreases for higher frequencies due to insufficient spatial resolution and partial masking of NLG noise by MLG and flap side edge sources. The acoustic results generated from the present simulations are compared to flight test data in our companion paper [28] to ascertain the capability of the computational approach in predicting the farfield noise signature of a full-scale aircraft with and without airframe noise reduction treatments.

Acknowledgments

References

[1] M. Basner, C. Clark, A. Hansell, J. I. Hileman, S. Janssen, K. Shepherd and V. Sparrow, "Aviation Noise Impacts: State of the Science," *Noise & Health,* vol. 19, no. 87, pp. 41-50, 2017.

[2] Boeing, [Online]. Available: http://www.boeing.com/resources/boeingdotcom/commercial/about-our-market/assets/downloads/cmo_print_2016_final_updated.pdf. [Accessed 17 October 2017].

[3] M. R. Khorrami, J. W. M. Humphreys and D. P. Lockard, "An Assessment of Flap and Main Landing Gear Noise Abatement," in *AIAA Paper 2015-2987*, 2015.

[4] M. R. Khorrami, D. P. Lockard, J. W. M. Humphreys and P. A. Ravetta, "Flight-Test Evaluation of Airframe Noise Mitigation Technologies," in *Paper to be presented at the AIAA/CEAS Aeroacoustics Conference in Atlanta, Georgia, June 2018*, 2018.

[5] E. Baumann and E. Waggoner, "Flight and Ground Operations in Support of Airframe Noise Reduction Tests," *2018 AIAA/CEAS Aeroacoustics Conference,,* Vols. AIAA paper 2018-2970, 2018.

[6] M. R. Khorrami, E. Fares and D. Casalino, "Towards Full Aircraft Airframe Noise Prediction: Lattice Boltzmann Simulations," *AIAA Paper 2014-2481,* 2014.

[7] E. Fares, D. Casalino and M. R. Khorrami, "Evaluation of Airframe Noise Reduction Concepts via Simulations Using a Lattice Boltzmann Approach," *AIAA Paper 2015-2988,* 2015.

[8] M. R. Khorrami and E. Fares, "Simulation-Based Airframe Noise Prediction of a Full-Scale Full Aircraft," *AIAA Paper 2016-2706,* 2016.

[9] J. Appelbaum, B. Duda, E. Fares and M. R. Khorrami, "Airframe Noise Simulations of a Full-Scale Aircraft," *AIAA Paper 2018-2973,* 2018.

[10] R. J. Ferris, J. Appelbaum and M. R. Khorrami, "Simulations of a Full-Scale Aircraft with Installed Airframe Noise Reduction technologies," *AIAA Paper 2018-2974,* 2018.

[11] M. R. Khorrami, P. A. Ravetta, D. P. Lockard, B. Duda and R. Ferris, "Comparison of Measured and Simulated Acoustic Signatures for a Full-Scale Aircraft with and without Airframe Noise Abatement," *AIAA Paper 2018-2975,* 2018.

[12] H. Chen, "Volumetric Formulation of the Lattice-Boltzmann Method for Fluid Dynamics: Basic Concept," *Physical Review E,* vol. 58, no. 3, pp. 3955-3963, 1998, doi: dx.doi.org/10.1103/PhysRevE.58.3955.

[13] H. Chen, C. Texeira and K. Molvig, "Realization of Fluid Boundary Condition via Discrete Boltzmann Dynamics," *International Journal of Modern Physics C,* pp. 1281-1292, 1998.

[14] H. Chen, S. Kandasamy, S. Orszag, R. Shock, S. Succi and V. Yakhot, "Extended Boltzmann Kinetic Equation for Turbulent Flows," *Science,* no. 301, pp. 633-636, 2003.

[15] S. Chen and G. Doolen, "Lattice Boltzmann Method for Fluid Flows," *Annual Review of Fluid Mechanics,* vol. 30, pp. 329-364, 1998.

[16] E. Fares and S. Nölting, "Unsteady Flow Simulation of a High-Lift configuration using Lattice-Boltzmann Approach," *AIAA Paper 2011-869,* 2011.

[17] D. Casalino, S. Noelting, E. Fares, T. Van de Ven, F. Perot and G. Bres, "Towards Numerical Aircraft Noise Certification: Analysis of a Full-Scale Landing Gear in Fly-Over Configuration," *AIAA Paper 2012-2235,* 2012.

[18] D. Casalino, A. F. P. Ribeiro, E. Fares, S. Nölting, A. Mann, F. Perot, Y. Li, P.-T. Lew, C. Sun, P. Gopalakrishnan, R. Zhang, H. Chen and K. Habibi, "Towards Lattice-Boltzmann Prediction of Turbofan Engine Noise," *AIAA Paper 2014-3101,* 2014.

[19] H. Chen, S. Chen and W. H. Matthaeus, "Recovery of the Navier-Stokes equations using a lattice-gas Boltzmann method," *Physical Review A,* no. 45, pp. R5339-R5342, 1992.

[20] Y. H. Qian, D. D'Humières and P. Lallemand, "Lattice BGK Models for Navier-Stokes Equation," *Europhysics Letters,* vol. 17, pp. 479-484, 1992.

[21] V. Yakhot and S. Orszag, "Renormalization Group Analysis of Turbulence," *Journal of Scientific Computing,* vol. 1, no. 2, pp. 3-51, 1986, doi: 10.1007/BF01061452.

[22] E. Fares, "Unsteady Flow Simulation of the Ahmed Reference Body using a Lattice Boltzmann Approach," *Journal of Computers and Fluids,* no. 35, pp. 940-950, 2006,.

[23] J. E. Hawkings and D. L. Ffowcs Williams, "Sound Generation by Turbulence and Surfaces in Arbitrary Motion," *Philosophical Transactions of the Royal Society of London. Series A, Mathematical and Physical Sciences,* vol. 264, no. 1151, pp. 321-342, 1969.

[24] F. Farassat and G. Succi, "The Prediction of Helicopter Discrete Frequency Noise," *Vertica,* vol. 7, no. 4, pp. 309-320, 1983.

[25] A. Najafi-Yazdi, G. Brès and L. Mongeau, "An Acoustic Analogy Formulation for Moving Sources in Uniformly Moving Media," *Proceeding of The Royal Society of London A,* vol. 467, no. 2125, pp. 144-165, 2011.

[26] ICAO, Environmental Protection, Annex 16 to the Convention on International Civil Aviation, Vol. 1: Aircraft Noise, Appendix 2.

[27] M. R. Khorrami, D. P. Lockard, W. M. J. Humphreys and P. A. Ravetta, "Flight-Test Evaluation of Landing Gear Noise Reduction Technologies," *Paper to be presented at the AIAA/CEAS Aeroacoustics Conference in Delft, The Netherlands,* May 2019.

[28] M. R. Khorrami, P. A. Ravetta, D. P. Lockard, B. Duda and R. J. Ferris, "Measured and Simulated Acoustic Signature of a Full-Scale Aircraft with Airframe Noise Reduction Technology Installed," *Paper to be presented at the AIAA/CEAS Aeroacoustics Conference in Delft, The Netherlands,* May 2019.

[29] B. König, E. Fares, P. Ravetta and M. Khorrami, "A Comparative Study of Simulated and Measured Main Landing Gear Noise for Large Civil Transports," *AIAA Paper 2017-3013,* 2017.

[30] S. Kota, P. Flick and F. Collier, "Flight Testing of the FlexFloilTM Adaptive Compliant Trailing Edge," *AIAA Paper 2016-0036,* 2016.

[31] E. Fares, B. Duda and M. R. Khorrami, "Airframe Noise Prediction of a Full Aircraft in Model and Full Scale Using a Lattice Boltzmann Approach," in *AIAA Paper 2016-2707,* 2016.

[32] E. J. Miller, J. Cruz, S. -F. Lung, S. Kota, G. Ervin, K. -J. Lu and P. Flick, "Evaluation of the Hinge Moment and Normal Force Aerodynamic Loads from a Seamless Adaptive Compliant Trailing Edge Flap in Flight," *AIAA Paper 2016-0038,* 2016.